Large Signal Modeling of HBT's Including Self-Heating and Transit Time Effects

P. Chris Grossman, *Student Member, IEEE,* and John Choma, Jr., *Fellow, IEEE*

Abstract—**A physically based, large signal HBT model is presented to account for the time dependence of the base, collector, and emitter charging currents, as well as self heating effects. The model tracks device performance over eight decades of current. As such, the model can be used as the basis of SPICE modeling approximations, and to this end, examples are presented. A thesis for the divergence of high frequency large signal SPICE simulations from measured data is formulated, inclusive of a requisite empirical equation for the base-collector junction capacitance.**

Keywords—**Heterojunction; model; time; circuit; capacitance; bipolar; HBT; charge; thermal; recombination; transistor; transit; SPICE; junction; electroluminescence.**

I. Introduction

HETEROJUNCTION bipolar transistors (HBT's) are used in a wide variety of analog and digital circuits. The ability to synthesize on-chip inductors and microstrip structures on the semi-insulating substrate of $GaAl_xAs_{1-x}$ devices make HBT's ideal for microwave applications.

The accurate prediction of large signal circuit performances requires a device model that is valid for a wide range of operating biases and signal frequencies. Existing SPICE [1], [2] bipolar transistor models, which are based on the Gummel–Poon model [3], do not address all effects which are key to the prediction of large signal HBT performance. These effects include the time dependence of the transit charge associated with the base and base-collector space charge regions (SCR's), monotonically increasing current gain versus collector current, and the effects of device self heating.

HBT models [4]–[6] predicated on Ebers–Moll theory [7] have been developed which account for the collector current versus base-emitter voltage. However these models do not match the base current versus base-emitter voltage characteristics of the device, since a flat current gain versus collector current characteristic is implicit to the Ebers–Moll model. The fundamental problem is that Ebers–Moll transistor models do not account for space charge and surface recombination, which largely limits the current gain of GaAlAs HBT's. Surface recombination, which is ignored in all existing circuit level models of HBT's, is negligible in all but the earliest of BJT's [7]–[9]. The immediate effect of surface recombination is analogous to the low current inefficiency of light emitting diodes (LED's) [10]–[12]. Thus the surface recombination current scales for HBT's as it does for LED's.

The base-collector capacitance equation used in SPICE does not match measured HBT device characteristics. The SPICE model fails to consider the effects of the collector contact layer, which limits the minimum base-collector capacitance.

A physically based, large signal HBT model is presented to account for the time dependence of the base, collector, and emitter charging currents. By including self heating and recombination effects, the model emulates the bias dependence of current gain over at least eight decades of current. The parameters of the proposed model scale with device dimensions.

The imperatives of every day engineering require that circuits be designed, simulated, and produced rapidly, with the tools at hand. Since the model presented here is not available at present in existing circuit simulation programs, a procedure for making do with those programs is necessary. For signal frequencies much less than the device gain-bandwidth product f_t, HBT macromodels formed with available SPICE elements can be configured. An example procedure is demonstrated.

The summary model description contained in this paper is aimed at the designer of HBT circuits and hence does not address in detail the physical effects involved in the operation of the device, but only describes their resulting electrical properties. S. Maas [13] has shown that the static components of the model accurately predict the low frequency IM distortion at 50 MHz.

All of the experimental work for this paper was conducted using TRW profile 9 HBT's (Fig. 1).

II. The Model

The large signal model (Fig. 2) is made up of diodes, resistors, voltage dependent capacitors, and time dependent current sources. Also included is a thermal circuit model [14]–[16] (Fig. 3) that dynamically modifies pertinent electrical parameters. Inherent to the model is the assumption that all of the volt-ampere charge character-

Manuscript received June 26, 1991; revised November 11, 1991. This work was supported primarily by TRW Internal Research and Development funds. It was also supported in part by a University of South Florida (USF) subcontract, No. 2114-033-LOA, in conjunction with a program funded to USF by the Defense Advanced Research Projects Agency (DARPA).

P. C. Grossman is with TRW Electronic Systems Group, Redondo Beach, CA 90278.

J. Choma is with the Department of Electrical Engineering-Electrophysics, University of Southern California, Los Angeles, CA 90089-0271.

IEEE Log Number 9105703.

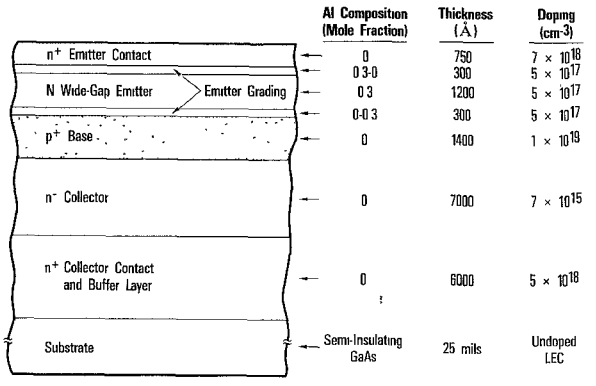

Fig. 1. TRW Profile 9 epitaxial HBT growth profile. Si is used as the *n* dopant. *Be* or *C* is used as the *p* dopant.

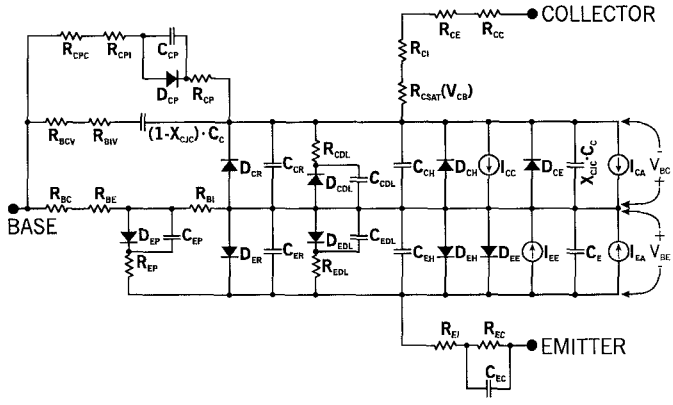

Fig. 2. Schematic diagram of the HBT large signal model. V_{BE} and V_{BC} are the voltages across the space charge regions, not the external device terminals.

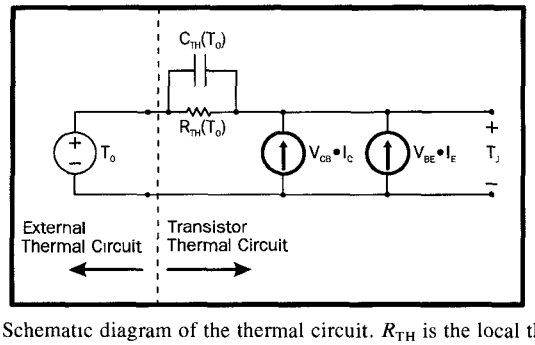

Fig. 3. Schematic diagram of the thermal circuit. R_{TH} is the local thermal resistance of the device. C_{TH} is adjusted to account for the local thermal time constant.

istics of all components of the device can be modeled with independent elements. This assumption is not strictly valid, since physical interactions couple various elements. Fortunately, such interactivity comprises only second order interest. The electrical model consists of diodes to model injection and recombination mechanisms, ohmic resistors, virtual resistors to model recombination limiting mechanisms, voltage dependent capacitors to model non-transit related charge storage, and current sources to represent both breakdown mechanisms and the time dependent collection of electrons from the neutral base.

The parameters R_{BC}, R_{CC}, and R_{CPC} are lateral contact resistances while R_{BI} and R_{CI} are spreading resistances. The elements R_{BE}, R_{CPI}, R_{CE}, R_{CSAT}, and R_{EI} are ohmic bulk resistors. The resistors R_{CP}, R_{EP}, R_{CDL}, and R_{EDL} model recombination limiting mechanisms.

The capacitors C_E and C_C, correspond to the base-emitter and base-collector junctions, respectively. C_{EP}, C_{ER}, C_{EDL}, C_{CP}, C_{CR}, and C_{CDL} are voltage dependent capacitors that model the charge storage corresponding to diodes represented by identical subscripts. C_{EC} is the Schottky junction capacitance of the emitter contact.

The temperature dependence of each of the model elements is described by empirical relationships, whose independent temperature variable is defined by the thermal circuit.

A. Diodes

The volt-ampere equations pertinent to all model diodes are identical in form. Examples are given only for diodes associated with electron injection and optical space charge recombination. The variable names for all remaining diodes are provided in Table I.

1) Electron Injection from the Emitter into the Base, D_{EE}: Diode D_{EE} models the injection of electrons from the emitter into the base. The physical mechanism for this injection may be classical diffusion, thermionic emission, or a combination of the two. In any case, the electron current I_F obeys the conventional Boltzman relationship [19]:

$$I_F(t) = I_{SF}\left(\exp\left(\frac{V_{BE}(t)}{N_F V_T}\right) - 1\right) \tag{1}$$

Because the base of an HBT is typically doped orders of magnitude higher than the base of an ordinary bipolar junction transistor, there are no conductivity modulation effects [8]. Thus, (1) is valid over the entire operating regime of the device.

The temperature dependence of the saturation current I_{SF} is described by two constants: the maximum saturation current $I_{SF\infty}$ and the saturation current temperature T_S. The currents I_{SF} and $I_{SF\infty}$, which are proportional to the base-emitter junction area A_E obey an equation of identical form:

$$\ln(I_{SF}) = \ln(I_{SF\infty}) - \frac{T_S}{T} \tag{2}$$

where temperature T and the parameter T_S are in °Kelvin. Parameter T_S is related to the activation energy Φ_S (in electron-volts) by a constant; namely,

$$\Phi_S = \frac{k}{q} T_S. \tag{3}$$

The ideality factor N_F is independent of temperature. For homojunctions, N_F is near unity; for heterojunctions it is usually in the range of 1.02 to 1.15.

2) Optical Recombination in the Base-Emitter Space Charge Region, D_{ER}: Diode D_{ER} models the optical recombination [10], [11], [20] in the base-emitter space

TABLE I
THE DIODES AND ASSOCIATED PARAMETERS OF THE LARGE SIGNAL HBT MODEL

Diode Name	Diode Current	Diode Voltage	Saturation Current	Saturation Current T	Ideality Factor	Linear Ideality Factor TC	Second Order Ideality Factor TC	Negligible	Scales with	Physical Mechanism Modeled	References
D_{EE}	I_F	V_{BE}	I_{SF}	T_S	N_F	—	—		A_E	Electron injection into the base from the emitter	4-7, 19
D_{EH}	I_{EH}	V_{BE}	I_{SEH}	T_{SEH}	N_{EH}	—	—	Yes	A_E	Hole injection into the emitter from the base	4-7, 19, 29-33
D_{EDL}	I_{EDL}	V_{EDL}	I_{SEDL}	T_{SEDL}	N_{EDL}	α_{EDL}	β_{EDL}	Use for marginal devices	A_E	Recombination through deep levels in the base-emitter SCR	10, 34-36
D_{ER}	I_{ER}	V_{BE}	I_{SER}	T_{SER}	N_{ER}	α_{ER}	β_{ER}		A_E	Optical recombination in the base-emitter SCR	18-21
D_{EP}	I_{EP}	V_{EP}	I_{SEP}	T_{SEP}	N_{EP}	α_{EP}	β_{EP}		P_E	Base-emitter perimeter recombination	10-12, 21-28
D_{CE}	I_{CE}	V_{BC}	I_{SCE}	T_{SR}	N_R	—	—		$\approx A_C$	Electron injection into the base from the collector	4-7, 19
D_{CH}	I_{CH}	V_{BC}	I_{SCH}	T_{SCH}	N_{CH}	—	—	usually	A_C	Hole injection into the collector from the base	4-7, 19
D_{CDL}	I_{CDL}	V_{CDL}	I_{SCDL}	T_{SCDL}	N_{CDL}	α_{CDL} Zero for homojunction	β_{CDL} Zero for homojunction	yes	A_C	Recombination through deep levels in the base-collector SCR	10, 34-36
D_{DR}	I_{CR}	V_{BC}	I_{SCR}	T_{SCR}	N_{CR}	α_{CR}	β_{CR}	yes	A_C	Optical recombination in the base-collector SCR	18-21
D_{CP}	I_{CP}	V_{CP}	I_{SCP}	T_{SCP}	N_{CP}	α_{CP} Zero for homojunction	β_{CP} Zero for homojunction		P_C	Base-collector perimeter recombination	10-12, 21-28

charge region (Fig. 4). This current is given by

$$I_{ER}(t) = I_{SER}\left(\exp\left(\frac{V_{BE}(t)}{N_{ER}V_T}\right) - 1\right). \quad (4)$$

In (4), the base-emitter optical saturation current I_{SER} is proportional to the base-emitter junction area A_E. The nonideal injection factor N_{ER} of the base-emitter optical recombination current is usually greater, but no less than, the ideality factor of the injected electron current, N_F. At room temperature, $1.1 < N_{ER} < 2.0$; typically $N_{ER} = 1.3$.

The dependence of N_{ER} on temperature follows the empirical expression,

$$N_{ER}(T) = N_{ER}(T_0)[1 + \alpha_{ER}\,\Delta T + \beta_{ER}\,\Delta T^2] \quad (5)$$

For most TRW HBT's, N_{ER} increases linearly with temperature [21] and β_{ER} is therefore set to zero. For computational convenience a reference temperature of $T_0 = 0°K$ is usually chosen.

B. Current Sources

1) Base Transport and the Collection of Injected Electrons, I_{CC} and I_{EE}: Recombination in the neutral base is modeled by the time dependent electron collection current sources, I_{CC} and I_{EE}. The current I_{CC} only collects a portion, α_F, of the injected electron current I_F. The remainder of the current $(1 - \alpha_F)I_F$ is the portion of the base current that accounts for recombination in the neutral base region. The parameter α_F is the base transport efficiency, not the product of base transport efficiency and emitter injection efficiency as in the Ebers–Moll model [7].

The Ramo–Schockley theorem [40] requires that the collected electron current I_{CC} be the spatial average of the current in the base-collector space charge region (Fig. 5).

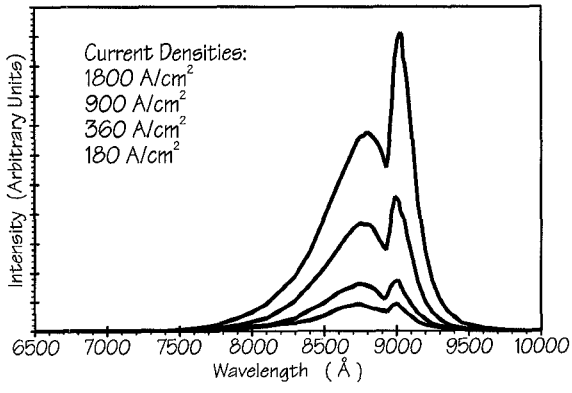

Fig. 4. Measured electroluminescence spectra from a profile 9 TRW HBT. The broad peak at 8750 Å is due to the optical recombination in the base-emitter space charge region. The narrow peak at 9020 Å is due to optical recombination in the neutral base region. The lack of a peak at 6700 Å shows that no holes are being injected into the wide band gap emitter. The spectra are uncorrected for the response of the S-1 photomultiplier detector.

Thus,

$$I_{CC} = \frac{1}{Z_{CC} - Z_{BC}}\int_{Z_{BC}}^{Z_{CC}} I(z)\,dz. \quad (6)$$

The average carrier velocity-vs-position in the base-collector space region may be found using Monte–Carlo simulations [41]–[43]. However, if a dual constant electron velocity profile (Fig. 6) is used to approximate the actual electron velocity-field profile in the base-collector space charge region, the collected electron current I_{CC} can be expressed as time integral in terms of τ_B the base transit time, τ_C the base-collector space charge region transit time, and τ_{OV} the ballistic region transit time. If the average electron overshoot velocity is v_{OV}, and the saturated electron velocity is v_{SAT}, the width of the base-collector space charge region is

$$W_C = Z_{CC} - Z_{BC} = \tau_{OV}v_{OV} + (\tau_C - \tau_{OV})v_{SAT} \quad (7)$$

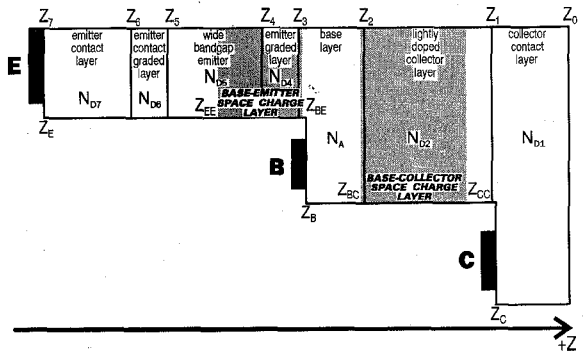

Fig. 5. HBT layer definitions. The Zs with numerical subscripts are the layer boundaries as grown. Z_{EE}, Z_{BE}, Z_{BC}, and Z_{CC} are the edges of the two space charge regions. After etching, Z_E is the top of the emitter mesa, Z_B is the top of the base mesa, and Z_C is the top of the substrate.

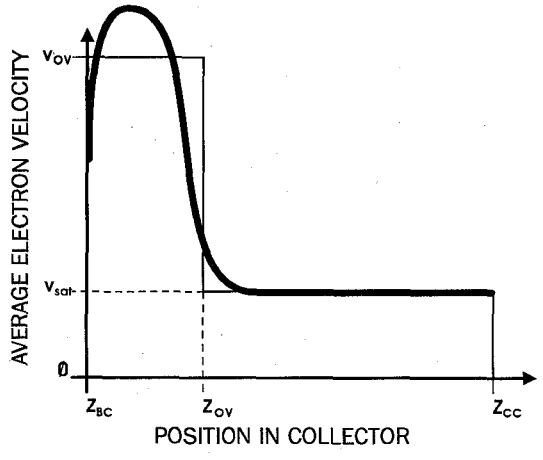

Fig. 6. Base-collector space charge region linearized electron velocity approximation. v_{OV} is the average velocity the overshoot region. v_{SAT} is the average saturation velocity.

With V_{AF} designating the forward Early voltage [1], [2], [34], [44], [45] and

$$I_{CZ}(\tau) = \alpha_F\left(1 - \frac{V_{BC}(\tau + \tau_B)}{V_{AF}}\right) \cdot I_{SF}\left(\exp\left(\frac{V_{BE}(\tau)}{N_F V_T}\right) - 1\right) \tag{8}$$

the collected electron current is

$$I_{CC}(t) = \frac{1}{W_C}\left(v_{OV}\int_{t-\tau_B-\tau_{OV}}^{t-\tau_B} I_{CZ}(\tau)\,d\tau + v_{SAT}\int_{t-\tau_B-\tau_C}^{t-\tau_B-\tau_{OV}} I_{CZ}(\tau)\,d\tau\right). \tag{9}$$

The resultant base charging current I_{QBF} is the difference of the portion of the injected electron current $\alpha_F I_F$ that will be collected and the collected electron current I_{CC}; that is,

$$I_{QBF}(t) = \alpha_F I_F(t) - I_{CC}(t). \tag{10}$$

Consider now an ideal device model (Fig. 2) in which all of the resistors and capacitors are of zero value, with

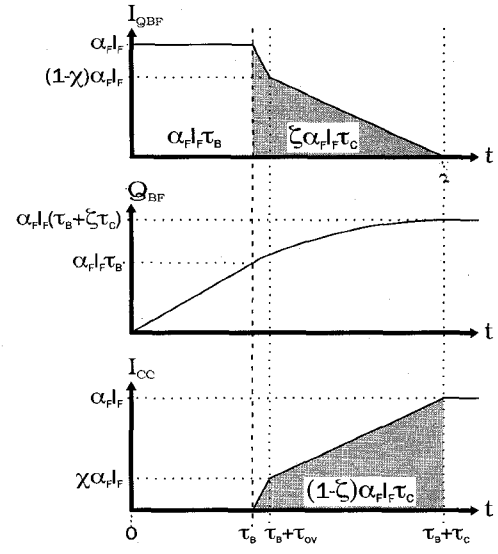

Fig. 7. Step response of the HBT model will all resistors and capacitors set to zero, infinite Early voltage, and the base-collector junction reverse biased. At $t = 0$ the emitter current step is I_F.

no breakdown effects, and the Early voltage V_{AF}, is infinitely large. With the base-collector junction reverse biased at a constant voltage and the base grounded, a current step is drawn from the emitter at time $t = 0$. The step response of the base charging current I_{QBF}, the stored base charge Q_{BF}, and the collected electron current I_{CC} are shown in Fig. 7. The current and stored charge reach their steady state values once the electrons have completely traversed the base-collector space charge region at $t = \tau_B + \tau_C$, thus

$$Q_{BF}(t) = \int_{t-\tau_B-\tau_C}^{t} I_{QBF}(\tau)\,d\tau. \tag{11}$$

The Gummel–Poon model in SPICE assumes that this base charge changes instantaneously with the base-emitter space charge bias V_{BE}. It may be seen from the above analysis that this assumption is a low frequency approximation. This is the reason large signal SPICE simulations, with frequency components approaching $1/2\pi(\tau_B + \tau_C)$, poorly match the measured data, even when all of the passive parasitic elements have been accounted for.

In SPICE, Q_{BF} is approximated using the following quasi steady state approximation,

$$I_C = \alpha_F I_F \tag{12}$$

$$Q_{BF} = I_C \tau_F \tag{13}$$

$$\chi = \frac{\tau_{OV} v_{OV}}{W_C} = \frac{\tau_{OV} v_{OV}}{\tau_{OV} v_{OV} + (\tau_C - \tau_{OV}) v_{SAT}} \tag{14}$$

$$\zeta = \frac{1}{2}\left(1 - \chi + \frac{\tau_{OV}}{\tau_C}\right) \tag{15}$$

$$\tau_F = \tau_B + \zeta\tau_C \tag{16}$$

where τ_F is the forward transit time.

Assuming a quasi-static base charge model, as in SPICE, $(I_C\tau_B)$ is the portion of the base charge needed to compensate for electrons traversing the base. $(I_C\zeta\tau_C)$ is the portion of the charge supplied to the base to compensate for the electrons traversing the base-collector space charge region.

The remaining compensation charge $[I_C(1-\zeta)\tau_C]$ for the electrons traversing the base-collector space charge region is supplied to the collector side of the region. In the step response of Fig. 7, the electrons entering the base-collector space charge region at $t = \tau_B$ do not emerge until $t = \tau_B + \tau_C$. Thus the collector current I_{CC} which flows from time $t = \tau_B$ until $t = \tau_B + \tau_C$, is the collector charging current. The quasi static SPICE model ignores the compensation charge stored in the collector. This is another source of error in large signal simulations, especially with HBT's whose collector transit time is usually much greater than the base transit time.

In a HBT, the base-collector space charge velocity profile is dependent on the base-collector bias. Thus, further work to define a circuit-oriented model velocity profiles remains.

It should be noted that the Kirk effect [46], also known as base push out, is usually precluded by the velocity overshoot in the collector region. Base push out has not been observed in any TRW HBT.

For the collection of electrons by the base-emitter space charge region that were injected from the collector into the base, a set of equations, analogous to those of I_{CC} exist for I_{EE}.

2) Base-Collector Avalanche Breakdown, I_{CA}: When the electrons traverse the base-collector space charge region, additional carriers are generated by avalanche multiplication [47]–[50]. This additional current due to avalanche breakdown [51] is represented by I_{CA}.

Avalanche multiplication produces electron-hole pairs and is a charge neutral process. If the time and spatial dependence of the additional avalanche current is ignored, no addition compensation charge needs to be supplied to the model. For simplicity, no attempt has been made to include the Ramo—Shockley effects or other time dependent details of the additional avalanche current. It is modeled as the product of the collected electron current I_{CC} and the empirical function $F_{CA}(V_{CB})$.

$$I_{CA}(t) = F_{CA}[V_{CB}(t)]\, I_{CC}(t). \tag{17}$$

The avalanche current increases as the reverse bias on the base-collector junction V_{CB} is increased. It is described by the empirical factors BV_{CBO} the base-collector junction breakdown voltage and N_{CA} the avalanche multiplication knee factor. When $V_{CB} \le 0$, the avalanche multiplication factor is zero. When $V_{CB} > 0$:

$$F_{CA}(V_{CB}) = \frac{\left(\dfrac{V_{CB}}{BV_{CBO}}\right)^{N_{CA}}}{1 - \left(\dfrac{V_{CB}}{BV_{CBO}}\right)^{N_{CA}}} \tag{18}$$

This function has a singularity when the $V_{CB} = BV_{CBO}$. Since this singularity causes convergence problems for circuit simulations, it is necessary to approximate the empirical avalanche factor F_{CA} by the following non singular Newton backward difference expansion [52].

$$\xi = \left(\frac{V_{CB}}{BV_{CBO}}\right)^{N_{CA}} \tag{19}$$

$$\begin{aligned} F_{CA} \cong\ & 24.4602\xi^2 - 212.8379\xi^3 + 1003.6601\xi^4 \\ & - 2649.2590\xi^5 \\ & + 3993.6680\xi^6 - 3202.8492\xi^7 + 1067.6184\xi^8. \end{aligned} \tag{20}$$

Even with this approximation, convergence problems may prevail. Thus, breakdown modeling should only be used when absolutely necessary, such as in cases were circuit distortion arising from operation near the breakdown region is critical. Also since the true time dependency in this formulation has been ignored, the reliability of the results for frequencies approaching $1/2\pi(\tau_B + \tau_C)$ are suspect. The temperature dependance BV_{CBO} and N_{CB} are characterized with linear temperature coefficients.

$$BV_{CBO} = BV_{CBO}(T_0)[1 + \alpha_{BV_{CBO}}\Delta T] \tag{21}$$

$$N_{CB} = N_{CB}(T_0)[1 + \alpha_{N_{CB}}\Delta T]. \tag{22}$$

3) Breakdown in the Base-Emitter Junction, I_{EA}: Breakdown in the base-emitter junction is due to Zener, not avalanche phenomena. Since a simple relation that defines the volt-ampere characteristics of Zener breakdown is lacking, the equations used to characterize I_{CA} are used to model the current I_{EA} as well.

C. Resistors

There are five types of resistors in the HBT model: bulk ohmic, lateral contact, vertical contact, spreading, and virtual. All resistances, except virtual resistances, can be calculated from the physical dimensions of the device and knowledge of the sheet resistance and contact conductance for various layers in the device (Table II). Virtual resistors are used to fine tune the model to the measured characteristics of the device. All of the resistors in the model are described in Table III.

1) Bulk Ohmic Resistors: A bulk ohmic resistor is calculated using the classic resistance formula,

$$R_{bulk} = \rho\frac{L}{A} = R_S\frac{L}{W}. \tag{23}$$

2) Vertical Contact Resistors: A vertical contact resistance occurs when the current flows normally through a contact surface. In HBTs, such resistances prevail for the emitter contact and the base contact resistance in series with the extrinsic base-collector capacitance. The vertical contact resistance is defined as

$$R_{vertical\_contact} = \frac{1}{AG_C} \tag{24}$$

TABLE II
TYPICAL SHEET RESISTANCE AND CONTACT CONDUCTANCE VALUES FOR TRW PROFILE 9 HBTs

Symbol	Value at $T_0 = 25°C$	Units	Linear Temperature Coefficient $\alpha_R(1/°C)$	Second Order Temperature Coefficient $\beta_R((1/°C)^2)$	Description
R_{SE}	113.0	Ω/■	$6.48 \cdot 10^{-5}$	0	Emitter contact layer sheet resistance
R_{SB}	560.0	Ω/■	$3.451 \cdot 10^{-3}$	0	Base layer sheet resistance
R_{SC}	11.20	Ω/■	$6.17 \cdot 10^{-4}$	0	Collector contact layer sheet resistance
G_{EC}	$6.17 \cdot 10^{5}$	$1/\Omega\text{-cm}^2$	$2.202 \cdot 10^{-3}$	$1.4 \cdot 10^{-5}$	Emitter contact conductance
G_{BC}	$3.45 \cdot 10^{5}$	$1/\Omega\text{-cm}^2$	$8.41 \cdot 10^{-4}$	0	Base contact conductance
G_{CC}	$5.00 \cdot 10^{5}$	$1/\Omega\text{-cm}^2$	$1.082 \cdot 10^{-3}$	$1.32 \cdot 10^{-5}$	Collector contact conductance

TABLE III
THE RESISTORS OF THE LARGE SIGNAL HBT MODEL

Symbol	Resistor Type	Negligible	Description
R_{BC}	Lateral contact		Lateral base contact resistance
R_{BE}	Bulk ohmic		Extrinsic base resistance
R_{BI}	Spreading		Intrinsic base spreading resistance
R_{EP}	Virtual	Yes	Base-emitter perimeter recombination limiting resistor
R_{EDL}	Virtual	Yes	Base-emitter deep level recombination limiting resistor
R_{EI}	Bulk ohmic	Yes	Intrinsic vertical emitter resistance
R_{EC}	Vertical contact		Vertical emitter contact resistance
R_{BCV}	Vertical contact	Yes	Vertical base contact resistance in series with the extrinsic base-collector capacitance
R_{BIV}	Bulk ohmic	Yes	Vertical intrinsic base resistance in series with the extrinsic base-collector capacitance
R_{CPC}	Lateral contact	Yes	Base-collector perimeter lateral base contact resistance
R_{CPI}	Bulk ohmic	Yes	Base-collector perimeter extrinsic base resistance
R_{CP}	Virtual	Yes	Base-collector perimeter recombination limiting resistance
R_{CDL}	Virtual	Yes	Base-collector space charge deep level recombination limiting resistor
R_{CSAT}	Bulk ohmic	Yes	Vertical resistance of the lightly doped collector layer (This is a function of V_{BC})
R_{CI}	Spreading		Collector spreading resistance
R_{CE}	Bulk ohmic		Extrinsic collector resistance
R_{CC}	Lateral contact		Lateral collector contact resistance

where A is the area of the contact, and G_C is the contact conductance per unit area.

3) Lateral Contact Resistors: A lateral contact resistance corresponds to the flow of sheet current that either enters or leaves a contact in parallel with the contact surface. Part of the resistance is due to the contact, and part of the resistance is due to the sheet spreading resistance.

For a contact length L and width W, the lateral contact resistance R_{LC} is

$$R_{LC} = \frac{\sqrt{\frac{R_S}{G_C}}}{W \tanh\left(\frac{L}{L_C}\right)} \tag{25}$$

where the contact characteristic length L_C is defined in terms of the contact conductance per unit area G_C and the layer sheet resistance R_S.

$$L_C \equiv \sqrt{\frac{1}{G_C R_S}}. \tag{26}$$

This result reveals an important layout guideline. In particular, note that little reduction in contact resistance is gained by making the length L wider than two contact characteristic lengths.

4) Spreading Resistors: A spreading resistance occurs when current enters a sheet region and is withdrawn normally with a constant current density. In HBT's, spreading resistances are manifested in the base layer under the

emitter mesa and in the collector contact layer under the base mesa. Because the doping is high and the resistivity is low in both these regions, the requisite spreading resistance calculations are accurate. Moreover, emitter crowding [34] which is significant in conventional BJT's, is negligible in most HBT's.

The spreading resistance R_{IS} of a region of width W, length L, sheet resistance R_S, and current entering from one side is defined as the average lateral voltage drop through the region divided by the current entering the region. The resultant spreading resistance is one third that of the bulk ohmic resistance of the region [53]. Hence,

$$R_{IS} = \frac{\frac{1}{L}\int_0^L V(x)\,dx}{I} = \frac{R_S L}{3W}. \tag{27}$$

If the current enters the region on two sides, as it does for the base resistance R_{BI}, this value is reduced by a factor of four since there are two parallel paths of one half the length.

5) Virtual Resistors: Virtual resistors are used to model the limiting of recombination mechanisms at high bias levels [27]. In most cases they are defaulted to zero.

D. Capacitors

Capacitors are used to model non-transit related charge storage mechanisms in the large signal model. Depletion capacitors are included for the base-emitter (C_E), base-collector (C_C), and Schottky emitter contact depletion regions (C_{EC}).

The remaining capacitances are defined in terms of effective lifetimes for the corresponding charge storage mechanisms. Unfortunately, the individual charge storage mechanisms are not easily separated from one another. Numerical simulations [54] using SEDAN depicts the combined lumped effects of all of the capacitances and with interpretation, some of the individual contributions may be understood. In general there are no simple equations to describe each capacitance element.

1) Base-Collector Depletion Capacitance, C_C: The base-collector junction of the TRW HBT is an abrupt homojunction. The base layer consists of a single homogeneous heavily doped layer. The collector is made up of two homogeneous layers: the lightly doped collector layer, and the collector contact layer.

Because the collector is made up of two regions, there are two regions of base-collector capacitance. The first region of base-collector capacitance corresponds to the collector edge of the depletion region in the lightly doped collector layer. The second is associated with the collector edge of the depletion region in the collector contact layer. These regions are referred to as I and II, respectively.

a) Region I; $Z_{CC} < Z_1$: This is the region in which the collector side of the base-collector depletion layer is inside the lightly doped collector layer. The width of the depletion region is $(Z_{CC} - Z_{BC})$ as defined in equation (28). The voltage V_{JC} is the built-in potential between the base and the lightly doped collector layers:

$$Z_{CC} - Z_{BC} = \left(1 + \frac{N_{D2}}{N_A + N_{D2}}\right) \cdot \sqrt{\frac{2\epsilon(V_{JC} - V_{BC}(N_A + N_{D2})}{qN_A N_{D2}}} \cong \sqrt{\frac{2\epsilon(V_{JC} - V_{BC})}{qN_{D2}}}. \tag{28}$$

A very good approximation of the base-collector capacitance per square centimeter is the dielectric constant divided by the depletion layer width; that is,

$$\left(\frac{C}{A}\right)_C = \frac{\epsilon}{Z_{CC} - Z_{BC}} \cong \frac{\sqrt{\frac{q\epsilon N_{D2}}{2V_{JC}}}}{\sqrt{1 - \frac{V_{BC}}{V_{JC}}}}. \tag{29}$$

Equations (28) and (29), and the base-collector junction area A_C yield the standard equation found in SPICE,

$$C_C = \frac{C_{JC}}{\left(1 - \frac{V_{BC}}{V_{JC}}\right)^{M_{JC}}} \tag{30}$$

The junction grading coefficient $M_{JC} = \frac{1}{2}$ and the zero bias base-collector junction capacitance C_{JC} is

$$C_{JC} = A_C\sqrt{\frac{q\epsilon N_{D2} N_A}{2V_{JC}(N_A + N_{D2})}} \cong A_C\sqrt{\frac{q\epsilon N_{D2}}{2V_{JC}}} \tag{31}$$

The peak electric field E_{MAX} occurs at the metallurgical junction. This field is defined analytically as

$$E_{MAX} = \frac{qN_A}{\epsilon}(Z_2 - Z_{BC}) \cong \sqrt{\frac{2qN_{D2}(V_{JC} - V_{BC})}{\epsilon}}. \tag{32}$$

b) Transition Point, Region I to Region II; $Z_{CC} = Z_1$: The transition point is where the base-collector depletion layer edge reaches the collector contact layer. The base-collector transition voltage V_{BCX} is found by stetting the width of the collector side of the depletion region equal to the width of the lightly doped collector and solving for the collector-base bias. Hence,

$$V_{BCX} = \frac{-qN_{D2}N_A(Z_1 - Z_2)^2}{2\epsilon(N_A + N_{D2})} + V_{JC} \cong \frac{-qN_{D2}(Z_1 - Z_2)^2}{2\epsilon} + V_{JC} \tag{33}$$

c) Region II; $Z_{CC} > Z_1$: In this region, the collector edge of the base-collector depletion layer is located in the collector contact layer. The profiling theorem states that the movement of the edge of the depletion region depends

only on the doping at the edges. Therefore the capacitance in this region may be described by a standard abrupt junction capacitance equation in which the doping at the edges of the depletion region appears, and the junction potential and zero bias capacitance are replaced with effective values.

The effective junction potential V_{JC2} is found by equating the collector side of the depletion layer width, at the crossover point, for the two regions:

$$V_{JC2} = V_{JC} + \frac{q(N_{D1} - N_{D2})(N_{D2} + N_A)(Z_1 - Z_2)^2}{2\epsilon(N_A + N_{D1})} \cong \frac{qN_{D1}N_A(Z_1 - Z_2)^2}{2\epsilon(N_A + N_{D1})}. \quad (34)$$

The capacitance of the two regions must be equal at the crossover point. Thus the effective zero bias junction capacitance C_{JC2} is found by equating the capacitance for the two regions at the crossover point. The result is

$$C_{JC2} = C_{JC} \cdot \frac{\left(1 - \frac{V_{BCX}}{V_{JC2}}\right)^{M_{JC2}}}{\left(1 - \frac{V_{BCX}}{V_{JC}}\right)^{M_{JC}}} \cong \frac{C_{JC}}{\left(1 - \frac{V_{BCX}}{V_{JC}}\right)^{M_{JC}}}. \quad (35)$$

Because the effective junction potential in region II is usually on the order of several thousand volts, the capacitance in this region is essentially constant, and is effectively the minimum capacitance C_{Cmin} for the junction.

The peak electric field E_{MAX} remains at the metallurgical junction between the base and lightly doped collector layer, Z_2. This peak field is given by

$$E_{MAX} = \frac{qN_AN_{D1}}{\epsilon(N_A + N_{D1})}\left(\sqrt{\frac{2\epsilon(V_{JC2} - V_{BC})(N_A + N_{D2})}{qN_AN_{D2}}} - \left(1 - \frac{N_{D2}}{N_{D1}}\right)(Z_1 - Z_2)\right). \quad (36)$$

d) Equations for Both Regions I & II: In the actual HBT, the capacitance-vs-voltage curve does not make a sharp transition when the base-collector voltage reaches V_{BCX}. Instead, the capacitance makes a smooth transition. The actual base-collector depletion capacitance for any base-collector bias fits the following empirical equation. The empirical factor N_{CC} is about 7 for MBE profile 9 (see Fig. 8).

$$C_C = \left(\left(\frac{C_{JC}}{\left(1 - \frac{V_{BC}}{V_{JC}}\right)^{M_{JC}}}\right)^{N_{CC}} + \left(\frac{C_{JC2}}{\left(1 + \frac{V_{BC}}{V_{JC2}}\right)^{M_{JC2}}}\right)^{N_{CC}}\right)^{1/N_{CC}}. \quad (37)$$

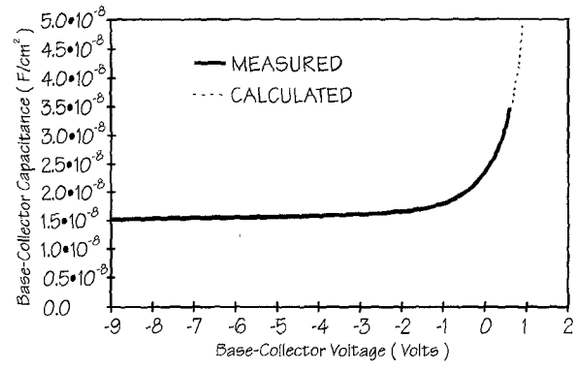

Fig. 8. Base-collector junction capacitance per unit area for a TRW profile 9 HBT.

Since the base-collector depletion capacitance in region II is essentially constant, the following expression, which is simpler than (37), incurs no significant loss in accuracy:

$$C_C \cong \left(\left(\frac{C_{JC}}{\left(1 + \frac{V_{BC}}{V_{JC}}\right)^{M_{JC}}}\right)^{N_{CC}} + [C_{Cmin}]^{N_{CC}}\right)^{1/N_{CC}}. \quad (38)$$

The above equations apply when the base-collector junction is reverse biased or only slightly forward biased. When the base-collector junction is forward biased to a point where significant conduction occurs, $V_{BC} \geq F_C V_{JC}$, an approximation based on the one used in SPICE is substituted for the capacitance:

$$C_C(V_{BC}) = C_C(F_C V_{JC}) + \left(\frac{\partial C_C}{\partial V_{BC}}\right)_{F_C V_{JC}} [V_{BC} - F_C V_{JC}]. \quad (39)$$

When $V_{BC} \geq F_C V_{JC}$ and $V_{BC} >> V_{BCX}$, the base-collector capacitance is approximated by the SPICE modeling equation:

$$C_C = \frac{C_{JC}}{(1 - F_C)^{1 + M_{JC}}} \cdot \left(1 - F_C(1 + M_{JC}) + \frac{M_{JC}V_{BC}}{V_{JC}}\right). \quad (40)$$

2) Base-Emitter Depletion Capacitance, C_E: Because the emitter is also made up of two layers, the base-emitter depletion capacitance C_E is described by a similar set of equations.

3) Hole Storage in the Collector and Emitter, C_{CH} and C_{EH}: The effects of charge due to holes stored in the emitter and collector can be emulated with capacitors that are a function of bias and a fixed minority carrier lifetime. Because the heterojunction prevents the injection of holes into the emitter, hole storage in the emitter and the associated capacitance C_{EH} can be neglected. However, hole storage in the collector can limit switching speed when

TABLE IV
THE CAPACITORS OF THE LARGE SIGNAL HBT MODEL

Symbol	Voltage Dependence	Negligible	Description
C_E	V_{BE}		Base-emitter depletion capacitance
C_C	V_{BC}		Base-collector depletion capacitance
C_{EH}	V_{BE}	Yes	Diffusion capacitance due to holes stored in them emitter
C_{CH}	V_{BC}		Diffusion capacitance due to holes stored in the collector
C_{EC}		Yes	Depletion capacitance of the emitter contact Schottky junction (Since this capacitor bypasses a degenerative element it may be important, especially when the emitter contact resistance is high)
C_{EDL}	V_{EDL}	Yes	Capacitance due to charge storage in the deep levels in the base-emitter space charge region
C_{CDL}	V_{CDL}	Yes	Capacitance due to charge storage in the deep levels in the base-collector space charge region
C_{ER}	V_{BE}		Capacitance due to charge storage in dips in the conduction band in the base-emitter space charge region (This capacitance dominates at low current densities and limits the f_t of the HBT)
C_{CR}	V_{BC}	Yes	Capacitance due to charge storage in dips in the conduction and/or valence band in the base-collector space charge region
C_{EP}	V_{EP}	Yes	Capacitance due to charge storage associated with the emitter perimeter recombination
C_{CP}	V_{CP}	Yes	Capacitance due to charge storage associated with the collector perimeter recombination

the HBT is driven into hard saturation and is thus included. τ_{CH} is the effective lifetime for holes in the collector and C_{CH} is the capacitance due to the hole storage in the collector:

$$C_{CH} = \frac{\partial[\tau_{CH} I_{CH}(V_{BC})]}{\partial V_{BC}} \tag{41}$$

and for constant lifetime τ_{CH},

$$C_{CH} = \frac{\tau_{CH}}{N_{CH} V_T} I_{SCH}\left(\exp\left(\frac{V_{BC}}{N_{CH} V_T}\right) - 1\right). \tag{42}$$

4) Charge Storage in the Base-Emitter Space Charge Region, C_{ER}: SEDAN simulations with supporting f_t measurements have shown [54] that dominant base-emitter capacitance C_{ER}, at low currents, is due to charge storage in dips in the base-emitter space charge region conduction band. When fitting f_t curves to measured data, this capacitance appears to be constant. Therefore the following empirical equation is used to model C_{ER}. The constant k_{ER} is an empirical factor, normally about 20:

$$C_{ER}(V_{BE}) = C_{ER0}\frac{1}{2}\left(1 + \tanh\left(\frac{k_{ER}[V_{BE} - F_E V_{JE}]}{V_{JE}}\right)\right). \tag{43}$$

5) Other Capacitors: The remaining capacitors are normally neglected. They exist in the model so that anomalous device performance may be simulated. All of these capacitors are listed in Table IV.

III. TEMPERATURE EFFECTS

The combination of the low thermal conductivity of GaAs [55] and the high power densities of HBTs makes device self heating [15] a more pronounced problem than it is in Si BJT's. This impacts the use of HBT's as power devices [56] and severely limits their use in comparator circuits [57].

For temperature effect simulations, all elements of the electrical model are modified by the temperature output of the thermal subcircuit. The temperature dependence of the electrical model parameters for a typical TRW HBT are shown in Table V and Fig. 9.

The local thermal resistance R_{TH} of a 3 × 10 micron emitter $GaAl_xAs_{1-x}$ HBT on a GaAs substrate at 25°C is about 1100 °C/W (Fig. 10). The self heating time constant, $R_{TH} \cdot C_{TH}$, is about 1 μs.

This large thermal resistance has severe consequences on device operation. For a typical device with a V_{CE} of 3 V and a I_C of 5 mA a temperature rise of 16.5°C above the substrate temperature will occur. Given that V_{BE} changes about −1.4 mV/°C, the V_{BE} of the device will decrease 23.1 mV. If this transistor were one half of the differential pair in a balanced comparator, the worst case thermal offset would be 46.2 mV. The exact thermal offset will depend on the duty cycle and frequency of the input signal. Since the area of local self heating [14], [15] is confined to within a radius of 30 microns of the junction, there is minimal thermal coupling between devices. Henceforth, there no layout schemes to minimize HBT comparator thermal offset. Only designs which minimize

TABLE V
TYPICAL VALUES FOR MODEL PARAMETERS FOR TRW PROFILE 9 HBT's

Name	Value	Units	Description
$J_{SF\infty}$	13.1	A/cm^2	Maximum saturation current density for the electrons injected into the base from the emitter
T_S	18500	°K	Saturation current temperature for I_{SF}
$J_{SER\infty}$	70	A/cm^2	Maximum saturation current density for the base-emitter space charge optical recombination
T_{SER}	18200	°K	Saturation current temperature for I_{SER}
$(I/P)_{SEP\infty}$	70	A/cm	Maximum saturation current per unit perimeter for the base-emitter perimeter recombination
T_{SEP}	9500	°K	Saturation current temperature for I_{SEP}
$J_{SCE\infty}$	1.08	A/cm^2	Maximum saturation current density for the electrons injected into the base from the collector
T_{SCE}	18280	°K	Saturation current temperature for I_{SCE}
$(I/P)_{SCP\infty}$	0.1	A/cm	Maximum saturation current per unit perimeter for the base-collector perimeter recombination
T_{SCP}	10000	°K	Saturation current temperature for I_{SCP}
N_F	1.0205		The ideality factor for electrons injected into the base from the emitter
T_0	−273	°C	The reference temperature for the ideality factors
$N_{ER}(T_0)$	1.0205		Ideality factor of the base-emitter optical recombination
$\alpha_{N_{ER}}$	$5.444 \cdot 10^{-4}$	1/°C	Linear temperature coefficient for N_{ER}
$\beta_{N_{ER}}$	0	(1/°C)^2	Second order temperature coefficient for N_{ER}
$N_{EP}(T_0)$	2.3		Ideality factor of the base-emitter perimeter recombination
$\alpha_{N_{EP}}$	$-2.805 \cdot 10^{-4}$	1/°C	Linear temperature coefficient for N_{EP}
$\beta_{N_{EP}}$	0	(1/°C)^2	Second order temperature coefficient for N_{EP}
N_R	1		The ideality factor for electrons injected into the base from the collector
N_{CP}	1.95		Ideality factor of the base-collector perimeter recombination
α_F	0.99667		The base transport efficiency
BV_{CBO}	22.3	V	Base-collector junction breakdown voltage at 25°C
$\alpha_{BV_{CBO}}$	0.000937	1/°C	Linear temperature coefficient for BV_{CBO}
N_{CB}	4.5		Base-collector breakdown knee factor for all temperatures

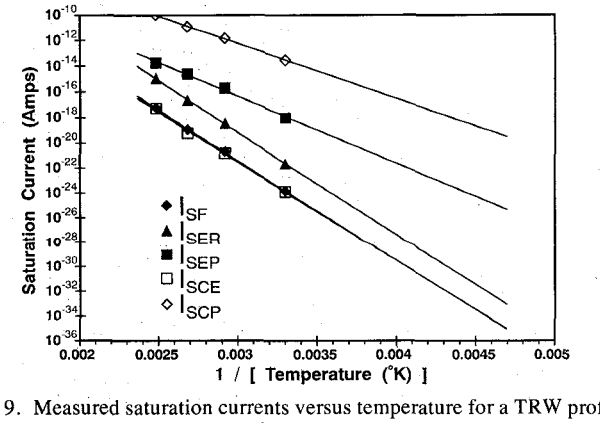

Fig. 9. Measured saturation currents versus temperature for a TRW profile 9 HBT.

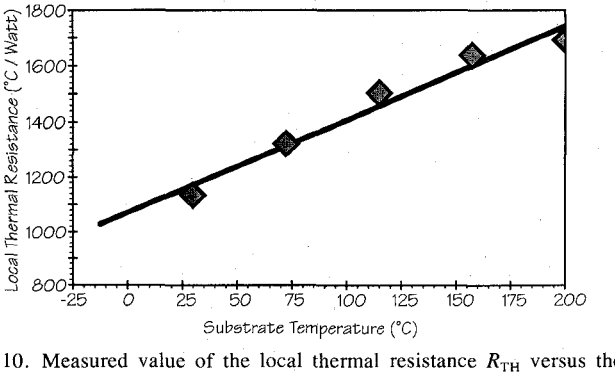

Fig. 10. Measured value of the local thermal resistance R_{TH} versus the substrate temperature for a 3 × 10 μm emitter TRW HBT.

the power dissipation in the sensing differential pair will make accurate HBT comparators.

The characteristic I_C/V_{CE} curves of an HBT with the apparent negative output impedance is also due to thermal effects. When the base is driven by a current source, as on a curve tracer, the slope of the output curve is entirely due to changes in dc current gain since the Early voltage, V_{AF}, is usually greater 1000 V. For most HBTs the current gain decreases as temperature increases. Thus as the de-

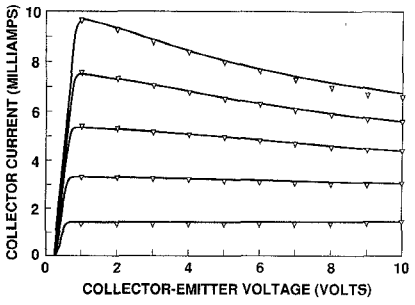

Fig. 11. Simulated versus measured I_C versus V_{CE} characteristics of a 3 × 10 μm TRW GaAlAs HBT. The base current is 20 μA per step. The triangles are the measured values.

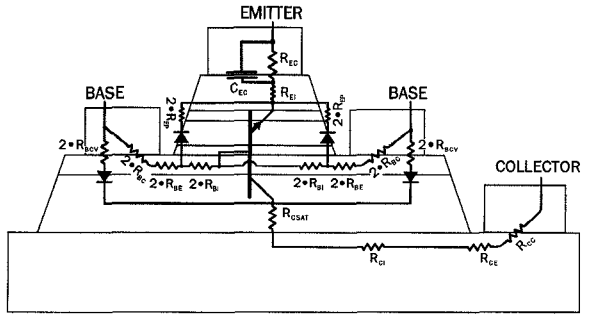

Fig. 12. An example SPICE macro model imposed on the HBT structure. The lateral contact resistors penetrate the contacts at 45°. The base-collector diodes represent the portion $(1 - X_{CJC})$ of the base-collector junction capacitance outside of the base resistance.

vice power dissipation increases, the gain drops as shown in Fig. 11.

IV. Approximation with a SPICE Macro Model

SPICE based simulators provide the ability to assemble macro models from stock elements (Fig. 12). An adequate HBT model can be assembled from the combination of the BJT, diode, resistor, and capacitor models in SPICE. The resulting model, while not including the effects of self heating, breakdown, or the time dependence of the base charge, will still yield very good results for frequencies at least two octaves below $1/2\pi(\tau_B + \tau_C)$.

One possible SPICE macro model presented here (Fig. 13) utilizes the BJT, diode, and resistor model. The BJT model simulates all of the device properties except those of base-emitter perimeter recombination and emitter contact resistance. Typical values for a TRW HBT can be found in Table VI.

A. BJT

Since high injection effects in the HBT can ignored, the knee current of the SPICE model is set to zero. With no high injection the forward collector current I_{CC} of the SPICE BJT model reduces to

$$I_{CC} = \left(1 - \frac{V_{BC}}{V_{AF}}\right) I_S \left(\exp\left(\frac{V_{BE}}{N_F V_T}\right) - 1\right) \quad (44)$$

where $I_S = \alpha_F I_{SF}$.

The Early voltage V_{AF} is on the order of 1000 V and may be ignored. However some circuits will not converge unless V_{AF} is included.

Since hole injection into the emitter is negligible, β_F in the BJT model only represents the effects of transport efficiency, α_F.

$$\beta_F = \frac{\alpha_F}{1 - \alpha_F}. \quad (45)$$

The resulting component of base current, due to recombination in the neutral base is

$$I_{\beta F} = \frac{I_S}{\beta_F}\left(\exp\left(\frac{V_{BE}}{N_F V_T}\right) - 1\right) \quad (46)$$

which is represented by diode $D_{\beta F}$.

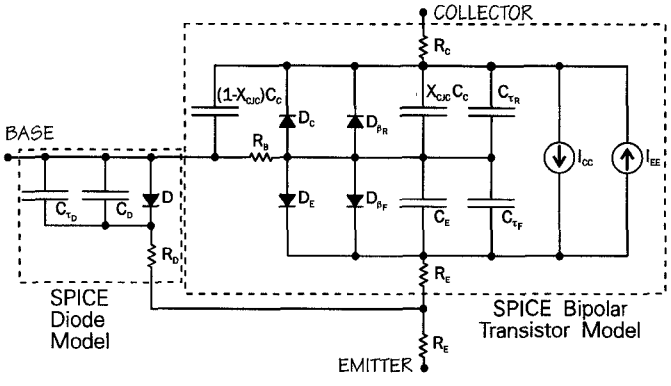

Fig. 13. SPICE macro model used to approximate HBT operation.

The base-emitter space charge optical recombination is simulated using the low current base-emitter recombination component of the SPICE BJT model,

$$I_{BE} = I_{SE}\left(\exp\left(\frac{V_{BE}}{N_E V_T}\right) - 1\right) \quad (47)$$

where $I_{SE} = I_{SER}$ and $N_E = N_{ER}$. The current I_{BE} is modeled by diode D_E.

The reverse electron current I_{EE} due to the base-collector being forward biased is exactly analogous with the forward electron current I_{CC}.

$$I_{EE} = \left(1 - \frac{V_{BE}}{V_{AR}}\right) I_{SR}\left(\exp\left(\frac{V_{BC}}{N_R V_T}\right) - 1\right) \quad (48)$$

where $I_{SR} = \alpha_R I_{SCE}$.

Because the base-collector junction is a homojunction, both the injected electrons ideality factor N_R and the injected holes ideality factor N_{CH}, are assumed to be identical. Hence injection efficiency is combined with the transport efficiency in the reverse current gain term,

$$\beta_R = \left(\frac{\alpha_R\left(\frac{I_{SCE}}{I_{SCE} + I_{SCH}}\right)}{1 - \alpha_R\left(\frac{I_{SCE}}{I_{SCE} + I_{SCH}}\right)}\right). \quad (49)$$

TABLE VI
TYPICAL SPICE MODEL PARAMETERS FOR A 3 × 10 μm EMITTER TRW PROFILE 9 HBT AT 25°C

Symbol	Value	Units	Description
R_E	11.0	Ω	Emitter contact resistance (External resistor, not in BJT model)
R_B	37.3	Ω	Total base resistance
R_C	6.42	Ω	Total collector resistance
I_S	$5.00 \cdot 10^{-25}$	A	Collector saturation current
I_{SE}	$7.70 \cdot 10^{-24}$	A	First base saturation current; B-E optical recombination
I_{SE2}	$4.00 \cdot 10^{-17}$	A	Second base saturation current; B-E perimeter recombination (Base-emitter diode)
I_{SR}	$4.14 \cdot 10^{-25}$	A	Reverse emitter saturation current
I_{SC}	$1.42 \cdot 10^{-14}$	A	Reverse base saturation current; B-C perimeter recombination
N_F	1.021		Collector current ideality factor
N_E	1 186		First base current ideality factor
N_{E2}	2.108		Second (base-emitter diode) ideality factor
N_R	1.000		Reverse emitter current ideality factor
N_C	1.950		Reverse base current ideality factor
β_F	300		Forward transport current gain
β_R	0.40		Maximum reverse current gain
τ_F	$4.3 \cdot 10^{-12}$	s	Forward transit time
$P_{\tau F}$	40	degrees	Excess phase factor
C_{JC}	$3.95 \cdot 10^{-14}$	F	Zero bias base-collector capacitance
M_{JC}	0.5		Collector capacitance grading coefficient
V_{JC}	1.18	V	Base-collector junction built in potential
X_{CJC}	0.220		Collector capacitance distribution factor
C_{JE}	$1.25 \cdot 10^{-13}$	F	Effective zero biased base-emitter capacitance for a forward biased junction
M_{JE}	0.51		Emitter capacitance grading coefficient
V_{JE}	1.45	V	Base-emitter junction built in potential
F_E	0.8		Linearization coefficient for the base-emitter capacitance

The resulting reverse base current, which is represented by diode $D_{\beta R}$, is

$$I_{\beta R} = \frac{I_{SR}}{\beta_R}\left(\exp\left(\frac{V_{BC}}{N_R V_T}\right) - 1\right) \tag{50}$$

Since the voltage drop across base resistance R_B in an HBT is usually negligible, the base-collector perimeter recombination diode can be moved inside R_B without any loss in accuracy. For this purpose, the base-collector perimeter recombination current component, represented by diode D_C, is

$$I_{BC} = I_{SC}\left(\exp\left(\frac{V_{BC}}{N_C V_T}\right) - 1\right) \tag{51}$$

where $I_{SC} = I_{SCP}$ and $N_C = N_{SCP}$.

The emitter resistance that is internal to the BJT model is set to zero. The emitter contact resistance is modeled by the external resistor, R_E. The base resistance in the BJT model is the sum of the lateral base contact resistance, the extrinsic base resistance, and the base spreading resistance. Hence,

$$R_B = R_{BC} + R_{BE} + R_{BI}. \tag{52}$$

Ignoring the bias dependent resistance $R_{CSAT}(V_{BC})$ of the lightly doped collector layer, the collector resistance is the sum of the collector spreading resistance, the extrinsic collector resistance, and the lateral collector contact resistance. Hence,

$$R_C = R_{CI} + R_{CE} + R_{CC}. \tag{53}$$

The characteristics of the base-collector capacitance C_C in the SPICE model does not match the that of the HBT. Thus, the SPICE model must approximate the actual capacitance as closely as possible. For most large signal simulations, the total charge that is pumped on and off base-collector capacitor is usually more important than the exact capacitance values. Therefore, the charge must be considered when choosing appropriate constants for the SPICE model. The resulting approximate base-collector capacitance is called C_{Ca}. The range of base-collector operating voltage for the device must be estimated to decide on a good capacitance compromise. Hence the total charge pumped onto and of the actual and approximate capacitors are equated,

$$\int_{V_{BC1}}^{V_{BC2}} C_C \, dV_{BC} \approx \int_{V_{BC1}}^{V_{BC2}} C_{Ca} \, dV_{BC} \tag{54}$$

Although the exact value of the capacitance is less important than the total charge, the mean squared error between the actual and approximate capacitances over the operating range should be kept to a minimum to ensure accurate circuit simulations. If this constraint is not applied, a fixed capacitance would satisfy the previous equation. The mean capacitance error over the bias range is

$$C_{error} = \sqrt{\frac{1}{(V_{BC2} - V_{BC1})}\int_{V_{BC1}}^{V_{BC2}} (C_C - C_{Ca})^2 \, dV_{BC}}. \tag{55}$$

X_{CJC} is the fraction of the base-collector capacitance under the emitter mesa. It is simply computed from the area of the base mesa A_C and emitter mesa A_E. Hence,

$$X_{CJC} = \frac{A_E}{A_C}. \tag{56}$$

The forward diffusion capacitance that is used to model charge storage due to transit effects is handled in SPICE by use of the forward transit time τ_F (16). The diffusion capacitance is

$$C_{\tau F} = I_{CC}\tau_F / V_T. \tag{57}$$

Since the SPICE model lacks elements to model the charge storage associated with the optical recombination in the base-emitter space charge region, that associated capacitance C_{ER} must be included in the SPICE base-emitter junction capacitance C_E. This approximation will work well while the transistor is forward biased, but will predict base-emitter capacitance that is too large when the device is not conducting. Without modifying the SPICE BJT model there is no way to fix this drawback. The values for the constants that describe C_E are fit to device f_t measurements.

B. The Diode

The base-emitter perimeter recombination in simulated by adding a diode from the base to the emitter terminals of the macro model. The capacitances in the diode are set to zero. The saturation current and ideality factor of the diode come directly from the full HBT model. They are called I_{SE2} and N_{E2} to keep the variable names consistent with previous work [21].

C. The DC Current Gain, β_{DC}

The dc current gain of HBTs is not a constant. The dc current gain β_{dc} typically increases with increasing collector current (Fig. 14). This is because the ideality factors of the base current components are larger than the ideality factor of the collector current.

The dc current gain is separated into components which account for each base current constituent. β_F is a constant which accounts for the recombination in the neutral base region, or base transport efficiency. β_1 accounts for the recombination in the base-emitter space charge region, and β_2 accounts for the perimeter recombination. For a given collector current, the dc current gain may be calculated as follows:

$$\beta_1 = \frac{I_S^{(N_F/N_E)}}{I_{SE}} I_C^{(1-(N_F/N_E))} \tag{58}$$

$$\beta_2 = \frac{I_S^{(N_F/N_{E2})}}{I_{SE2}} I_C^{(1-(N_F/N_{E2}))} \tag{59}$$

$$\frac{1}{\beta_{dc}} = \frac{1}{\beta_F} + \frac{1}{\beta_1} + \frac{1}{\beta_2}. \tag{60}$$

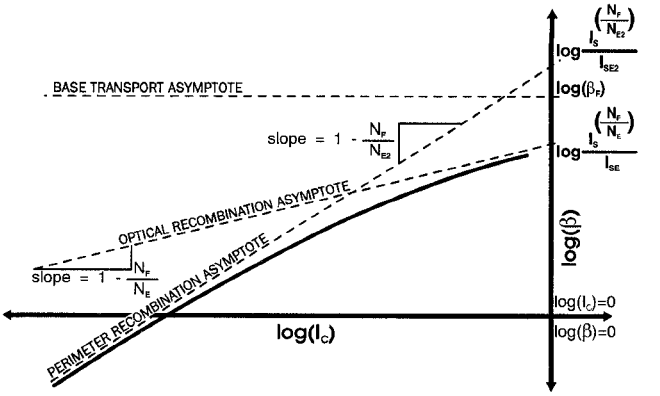

Fig. 14. Hypothetical plot of log (β_{dc}) versus log (I_C) for an HBT with all virtual resistors set to zero, and ignoring self heating effects.

The temperature dependence of each component of current gain must also be accounted for separately. For example, with constant collector current, the temperature coefficient of the base-emitter space charge optical recombination component of current gain is

$$\left(\frac{\frac{\partial\beta_1}{\partial T}}{\beta_1}\right)_{I_C} = -\left(\frac{T_{SE} - \left(\frac{N_F}{N_E}\right)T_S}{T^2} - \left(\frac{N_F}{N_E}\right)\alpha_{N_E}\ln\left(\frac{I_C}{I_S}\right)\right) \tag{61}$$

where T_S and T_{SE} are constants which describe the temperature dependence of I_S and I_{SE}. The ideality factor of the base current N_E is assumed to have a linear temperature coefficient α_{N_E}.

V. f_t Characterization

The dominant pole short circuit current gain-bandwidth product approximation f_t, is used as a figure of merit and for parameter extraction in BJT's and HBT's. Since f_t is a dominant pole approximation it is not the actual unity current gain of the transistor. Because of the effects of higher order zeros and collector delay [9], [58], the unity current gain frequency of an HBT can be over an octave higher than it's f_t. Thus care must be taken when determining f_t from measurements.

The standard textbook equations [45], [59], [60] for f_t ignore the contribution of the emitter resistance R_E. Neglecting R_E gives as much as a 15% error in the value of f_t for some HBTs. Using the variables from the previous SPICE model, f_t is defined as follows. The inverse of the small signal common emitter current gain is

$$\frac{1}{\beta_0} = \frac{\partial I_B}{\partial I_C} = \frac{1}{\beta_F} + \frac{N_F}{N_E\beta_1} + \frac{N_F}{N_{E2}\beta_2}. \tag{62}$$

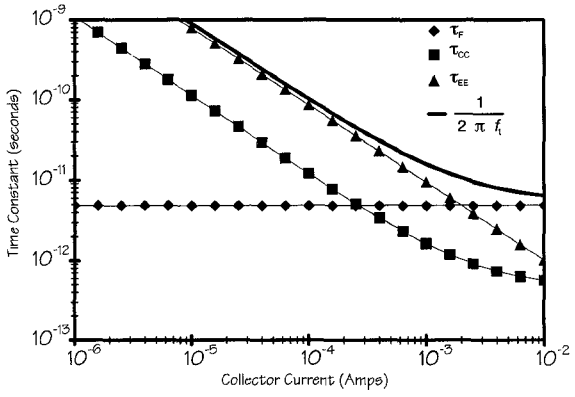

Fig. 15. Plot of the time constants versus collector current for a TRW profile 9, 3 × 10 μm emitter HBT. The base-collector bias V_{BC} was fixed at −1.5 V.

Hence, the small signal common base current gain is

$$\alpha_0 = \frac{\partial I_C}{\partial I_E} = \frac{\beta_0}{\beta_0 + 1}. \tag{63}$$

The small signal transconductance is

$$g_m = \frac{\partial I_C}{\partial V_{BE}} = \frac{I_C}{N_F V_T}. \tag{64}$$

Thus, including the effect of the emitter resistance, the short circuit current gain-bandwidth product is

$$f_t = \frac{1}{2\pi\left(\tau_F + \frac{C_E}{g_m} + \left(\frac{1}{g_m} + \frac{R_E}{\alpha_0}\right)C_C\right)}. \tag{65}$$

The base-collector capacitance charging time,

$$\tau_{CC} = \left(\frac{1}{g_m} + \frac{R_E}{\alpha_0}\right)C_C \tag{66}$$

is constrained to be no smaller than $((R_E/\alpha_0)\,C_C)$, by the inclusion of the emitter resistance in the equation.

The base-emitter capacitance charging time is defined as

$$\tau_{EE} = \frac{C_E}{g_m}. \tag{67}$$

The emitter contact resistance R_E, and the transconductance g_m, can be determined from dc measurements, device geometry, and bias conditions. The base-collector capacitance can be determined from C/V measurements, device geometry, and bias conditions. Thus by measuring f_t-versus-collector current, with a fixed base-collector bias voltage, the total base-emitter capacitance and forward transit time can be determined (Fig. 15) by adjusting C_E and τ_F (16) to fit measured log $(1/2\pi f_t)$ versus log (I_C) curves. The base-emitter capacitance C_E that results from this measurement will be the sum of all of the charge storage mechanisms associated with the base-emitter junction, not just the depletion capacitance.

VI. Conclusion

A physically based large signal HBT model has been presented that includes the effects of self heating, carrier transit, avalanche breakdown, and a new equation for empirical base-collector capacitance. A thesis for the deviation of the large signal SPICE simulations from the real device performance at high frequencies was proffered. Simple calculations are shown to bracket the limits of the thermal offset in a differential pair comparator.

An example of approximating the HBT model with a SPICE macro model was demonstrated, including an equation for f_t that accounts for emitter resistance. The SPICE model has been used at TRW in the past two years to accurately simulate circuits that operate below 3 GHz. Above this frequency the limitations of the time dependent charge limit accuracy for large signals.

Although the full model includes many effects not previously accounted for, more work remains. More rigorous results, or at least better empirical relationships, still need to be developed for the nontransit related charge storage, as well as for the bias dependence of the base-collector space charge carrier velocity profiles. In addition the model needs to be fully incorporated into a circuit simulation program such as SPICE.

Acknowledgment

I would like to acknowledge the enlightening discussions I have had with C. R. Crowell about the Ramo–Schockley theorem, and discussions about the SPICE model with W. Beall. Without the early support of R. Wiggins, and the later support of A. Oki, much of this work at TRW would not have been possible. I am grateful to them both.

References

[1] I. Getreu, *Modeling The Bipolar Transistor.* Beaverton: OR, Tektronix, 1977.

[2] P. Antognetti and G. Massobrio, *Semiconductor Device Modeling with SPICE.* New York: McGraw-Hill, 1988.

[3] H. K. Gummel and H. C. Poon, "An integral charge control model of bipolar transistors," *Bell Syst. Tech. J.*, vol. 49, pp. 827–852, May/June 1970.

[4] M. S. Lundstrom, "An Ebers–Moll model for the heterostructure bipolar transistor," *Solid-State Electron.*, vol. 29, no. 11, pp. 1173–1179, 1986.

[5] A. Marty, G. Rey, and J. P. Bailbe, "Electrical behavior of an NPN GaAlAs/GaAs heterojunction transistor," *Solid-State Electron.*, vol. 22, pp. 549–557, 1979.

[6] J. P. Bailbe, A. Marty, G. Rey, J. Tasselli, and A. Bouyahyaoui, "Electrical behavior of double heterojunction NpN GaAlAs/GaAs/GaAlAs bipolar transistors," *Solid-State Electron.*, vol. 28, no. 6, pp. 627–638, 1985.

[7] F. J. Biondi, Ed., *Transistor Technology, Vol. II.* Princeton, NJ: Van Nostrand, 1958.

[8] W. M. Webster, "On the variation of junction-transistor current-amplification factor with emitter current," *Proc. IRE*, vol. 42, pp. 914–920, June 1954.

[9] J. M. Early, "P-I-N-P and N-P-I-N junction transistor triodes," *Bell Syst. Tech. J.*, vol. 33, no. 3, pp. 517–533, May 1954.

[10] O. Leistiko, Jr. and C. A. Bittmann, "Surface effects of $GaAs_{0.6}P_{0.4}$ light emitting diodes," *Solid-State Electron.*, vol. 16, no. 12B, pp. 1321–1336, 1973.

[11] G. B. Stringfellow and D. Kerps, "Green-emitting diodes in vapor phase epitaxial GaP," *Solid-State Electron.*, vol. 18, pp. 1019–1028, 1975.
[12] G. B. Stringfellow, "Effect of surface treatment on the surface recombination velocity and diode leakage current in GaP," *J. Vacuum Science and Technology*, vol. 13, no. 4, pp. 908–913, July/Aug. 1976.
[13] S. A. Maas, 1990 Progress Report to TRW.
[14] P. R. Strickland, "The thermal equivalent circuit of a transistor," *IBM J.*, vol. 3, no. 1, pp. 35–45, Apr. 1959.
[15] R. T. Dennison and K. M. Walter, "Local thermal effects in high performance bipolar devices/circuits," in *Proc. 1989 IEEE Bipolar Circuits and Technology Meeting*, Sept. 1989, pp. 164–167.
[16] M. Latif and P. R. Bryant, "Multiple equilibrium points and their significance in the second breakdown of bipolar transistors," *IEEE J. Solid State Circuits*, vol. SC-16, pp. 8–14, Feb. 1981.
[17] P. T. Landsberg, "The band-band Auger effect in semiconductors," *Solid-State Electron.*, vol. 30, no. 11, pp. 1107–1115, 1987.
[18] H. Kressel and J. K. Butler, *Semiconductor Lasers and Heterojunction LED's*. New York: Academic, 1977.
[19] A. H. Marshank and R. Shrivastva, "Law of the junction for degenerate material with position-dependent band gap and electron affinity," *Solid-State Electron.*, vol. 27, pp. 567–571, 1979.
[20] H. Ito, "Generation-recombination current in the emitter-base junction of AlGaAs/GaAs HBTs," *Japan. J. Appl. Phys.*, vol. 25, no. 9, pp. 1400–1404, Sept. 1986.
[21] P. C. Grossman and A. Oki, "A large signal dc model for GaAs/$Ga_xAl_{1-x}As$ heterojunction bipolar transistors," in *Proc. 1989 IEEE Bipolar Circuits and Technology Meeting*, Sept. 1989, pp. 258–262.
[22] L. Jastrebski, H. C. Gatos, and J. Lagowski, "Observation of surface recombination variations in GaAs surfaces," *J. Appl. Phys.*, vol. 48, no. 4, pp. 1730–1731, Apr. 1977.
[23] C. H. Henry, R. A. Logan, and F. R. Merritt, "The effect of surface recombination on current in $Al_xGa_{1-x}As$ heterojunctions," *J. Appl. Phys.*, vol. 49, no. 6, pp. 3530–3542, June 1978.
[24] C.-C. Wu, J.-L. Ting, Si-C. Lee, and H.-H. Lin, "Studies of low-surface 2-kT recombination current of the emitter-base heterojunction of heterojunction bipolar transistors," *J. Appl. Phys.*, vol. 68, no. 4, pp. 1766–1771, Aug. 15, 1990.
[25] G. B. Strigfellow, "Effect of surface treatment on the surface recombination velocity and diode leakage current in GaP," *J. Vacuum Science and Technology*, vol. 13, no. 4, pp. 908–913, July/Aug. 1976.
[26] C. J. Sandroff, R. N. Nottenburg, J.-C. Bischoff, and R. Bhat, "Dramatic enhancement in the gain of a GaAs/AlGaAs heterostructure bipolar transistor by surface chemical passivation," *Appl. Phys. Lett.*, vol. 51, pp. 33–35, July 6, 1987.
[27] Y. S. Hiraoka, J. Yoshida, and M. Azuma, "Two-dimensional analysis of emitter-size effect on current gain for GaAlAs/GaAs HBT's," *IEEE Trans. Electron Devices*, vol. ED-34, no. 4, pp. 721–725, Apr. 1987.
[28] T. B. Stellwag, M. R. Melloch, M. S. Lundstrom, M. S. Carpenter, and R. F. Pierret, "Orientation-dependent perimeter recombination in GaAs diodes," *Appl. Phys. Lett.*, vol. 56, no. 17, pp. 1019–1028, Apr. 23, 1990.
[29] P. Enquist, G. W. Wicks, L. F. Eastman, and C. Hiltzman, "Anomalous redistribution of beryllium in GaAs grown by molecular Beam epitaxy," *J. Appl. Phys.*, vol. 58, no. 11, pp. 4130–4134, Dec. 1, 1985.
[30] D. L. Miller and P. M. Asbeck, "Be redistribution during growth of GaAs and AlGaAs by molecular beam epitaxy," *J. Appl. Phys.*, vol. 57, no. 6, pp. 1816–1822, Mar. 15, 1985.
[31] Y.-C. Pao, T. Hieri, and T. Cooper, "Surface effect-induced fast Be diffusion in heavily doped GaAs grown by molecular-beam epitaxy," *J. Appl. Phys.*, vol. 60, no. 1, pp. 1816–1822, July 1, 1986.
[32] W. S. Hobson, S. J. Pearton, and A. S. Jordan, "Redistribution of Zn in GaAs-AlGaAs heterojunction bipolar transistor structures," *Appl. Phys. Lett.*, vol. 56, no. 13, pp. 1251–1253, Mar. 26, 1990.
[33] C. Kusano, H. Masuda, K. Mochizuki, M. Kawada, and K. Mitani, "The effect on turn-on voltage (V_{BE}) of AlGaAs/GaAs HBT's due to the structure of the emitter-base heterojunction," *Japan. J. Appl. Phys.*, vol. 29, pp. 1399–1402, 1990.
[34] P. E. Gray, D. DeWitt, A. R. Boothroyd, and J. F. Gibbons, *Physical Electronics and Circuit Models of Transistors*. New York: Wiley, 1964.
[35] C.-T. Sah, R. N. Noyce, and W. Shockley, "Carrier generation and recombination in P-N junctions and P-N junction characteristics," *Proc. IRE*, vol. 45, pp. 1228–1243, Sept. 1957.
[36] H. F. Mataré, *Defect Electronics in Semiconductors*. New York: Wiley, 1971.
[37] M. S. Lundstrom, R. J. Schartz, and J. L. Grey, "Transport equations for the analysis of heavily doped semiconductor devices," *Solid-State Electron.*, vol. 24, pp. 195–202, 1981.
[38] K. Saito, T. Yamada, T. Akatsuka, T. Fukamachi, E. Tokumitsu, M. Konagai, and K. Takahashi, "Effect of heavy doping on band gap and minority carrier transport of AlGaAs/GaAs HBT's," *J. J. Appl. Phys.*, vol. 28, no. 11, pp. L2801–L2804, Nov. 1989.
[39] A. H. Marshak, "Transport equations for highly doped devices and heterostructures," *Solid-State Electron.*, vol. 39, no. 11, pp. 1089–1093, 1987.
[40] Z. Djurić, M. Smiljanić, and B. Radjenović, "The application of Ramo's theorem to impulse response calculation of a reach-through avalanche photodiode," *Solid-State Electron.*, vol. 27, no. 10, pp. 833–835, 1984.
[41] R. Katoh, M. Kurata, and J. Yoshida, "Self-consistent particle simulation for (AlGa)As/GaAs HBT's with improved base-collector structures," *IEEE Trans. Electron Devices*, vol. ED-36, no. 5, pp. 846–853, May 1987.
[42] P. I. Rockett, "Monte Carlo study of the influence of collector region velocity overshoot on the high-frequency performance of AlGaAs/GaAs heterjunction bipolar transistors," *IEEE Trans. Electron Devices*, vol. 35, no. 10, pp. 1573–1579, Oct. 1988.
[43] J. Hu, K. Tomizawa, and D. Pavlidis, "Transient Monte Carlo analysis and application to heterojunction bipolar transistor switching," *IEEE Trans. Electron Devices*, vol. 36, no. 10, pp. 2138–2145, Oct. 1989.
[44] J. M. Early, "Effects of space-charge layer widening in junction transistors," *Proc. IRE*, vol. 40, pp. 1401–1406, Nov. 1952.
[45] P. R. Gray and R. G. Meyer, *Analysis and Design of Analog Integrated Circuits*. New York: Wiley, 1977.
[46] C. T. Kirk, Jr., "A theory of transistor cutoff frequency (f_T) falloff at high current densities," *IRE Trans. Electron Devices*, vol. 9, pp. 164–174, Mar. 1962.
[47] J. Chen, G. B. Gao, D. Huang, J. J. Chyi, M. S. Ünlü, and H. Morkoç, "Photon emission from avalanche breakdown in the collector junction of GaAs/AlGaAs hetrojunction bipolar transistors," *Appl. Phys. Lett.*, vol. 55, no. 2, pp. 374–376, July 1989.
[48] J. J. Chen, G.-B. Gao, J.-I. Chyi, and H. Morkoç, "Breakdown behavior of GaAs/AlGaAs HBT's," *IEEE Trans. Electron Devices*, vol. 36, no. 10, pp. 2165–2172, Oct. 1989.
[49] A. G. Chynoweth, "Charge Multiplication Phenomena," *Semiconductors and Semimetals*, R. K. Willardson and A. C. Beer, Eds., vol. 4, pp. 263–325, 1968.
[50] S. M. Sze and G. Gibbons, "Avalanche breakdown voltages of abrupt and linearly graded p-n junctions in Ge, Si, GaAs, and GaP," *Appl. Phys. Lett.*, vol. 8, no. 5, Mar. 1, 1966.
[51] F. Severson, "A new LV_{CEO} SPICE model," in *Proc. 1986 IEEE Bipolar Circuits and Technology Meeting*, pp. 77–78, 1986.
[52] J. Choma, Jr., *Electrical Networks: Theory and Analysis*. New York: Wiley-Interscience, 1985, pp. 342–348.
[53] A. S. Grove, *Physics and Technology of Semiconductor Devices*. New York: Wiley, 1967.
[54] M. Hafizi, C. R. Crowell, and M. E. Kim, "Improved current gain and FT through doping profile selection, in linearly graded HBT's," *IEEE Trans. Electron Devices*, vol. 37, no. 8, pp. 1779–1788, 1990.
[55] J. S. Blakemore, "Semiconducting and other major properties of gallium arsenide," *J. Appl. Phys.*, vol. 53, no. 10, pp. R123–R181, Oct. 1982.
[56] G.-B. Gao, M.-Z. Wang, X. Gui, and H. Morkoç, "Thermal design studies of high-power heterojunction bipolar transistors," *IEEE Trans. Electron Devices*, vol. 36, no. 5, pp. 854–863, May 1989.
[57] K.-C. Wang, P. M. Asbeck, M.-Chung, F. Chang, D. L. Miller, Gerard J. Sullivan, J. J. Corcoran, and T. Hornak, "Heating effects on the accuracy of HBT voltage comparators," *IEEE Trans. Electron Devices*, vol. ED-34, no. 8, pp. 1729–1735, Aug. 1987.
[58] F. N. Trofimenkoff, "Collector depletion region transit time," *Proc. IEEE*, vol. 52, no. 1, pp. 86–87, Jan. 1964.
[59] D. J. Roulston, *Bipolar Semiconductor Devices*. New York: McGraw-Hill, 1990.
[60] S. M. Sze, *Physics of Semiconductor Devices*. New York: Wiley, 1981.

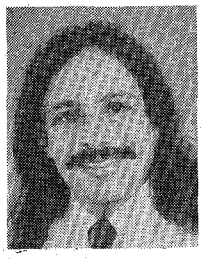

P. Chris Grossman (S'91) earned the B.S.E.E. and M.S.E.E. degrees in 1983 and 1985, respectively, from the University of Southern California (USC) where he is currently completing his Ph.D. dissertation. It is titled "Large Signal Models for Heterojunction Bipolar Transistors."

Since 1987, he has been a Senior Member of the Technical Staff at TRW Electronic Systems Group in Redondo Beach, CA, working on modeling, reliability, failure analysis, and test procedures for HBT's. His models are the used for most of the HBT integrated circuits designed at TRW. He has also been a research/teaching assistant at USC since 1983, where he has done research on oscillator design principles and magnetic effects in FETs. From 1979–1983 he was employed by Display Electronics Department of Hughes Aircraft Radar Systems Group, in El Segundo, Ca., where he designed a digital raster generator and CPU board for the F14 weapons control system. His interests include analog, microwave, and high speed digital circuit design, integrated device modeling, and power conversion circuits.

Mr. Grossman is a member of Eta Kappa Nu.

John Choma, Jr. (S'61–M'64–SM'76–F'91) earned the B.S., M.S., and Ph.D. degrees in electrical engineering from the University of Pittsburgh in 1963, 1965, and 1969, respectively.

He is currently a Professor of Electrical Engineering at the University of Southern California (USC) where he teaches undergraduate courses in electrical circuits and graduate courses in analog electronics. He consults in the areas of wideband analog and high speed integrated circuit design. Prior to joining USC in 1980, he was a Senior Staff Design Engineer in the TRW Microelectronics Center in Redondo Beach, California. While at TRW, he taught as Senior Lecturer in the Department of Electrical Engineering of the California Institute of Technology. His research interests include wideband analog and high-speed digital integrated circuit design, behavioral analysis of electronic systems, and integrated device modeling.

Dr. Choma is the author or co-author of 80 journal and conference papers, the author of a Wiley Interscience text on electrical network theory and a forthcoming Richard D. Irwin text on electronic circuit design, and the co-editor of a forthcoming Butterworth-Heinemann handbook on integrated circuit design. He is the recipient of several teaching awards and is currently one of only five faculty at USC to be named "Teaching Fellow" in the Center for Teaching Excellence.